

Journal of
***Mechanics of
Materials and Structures***

**AN OFF-RESONANCE SYNCHRONOUS VIBRATION
BASED METHOD FOR ROTOR SYSTEM DAMAGE
DETECTION**

Huageng Luo, Hector Rodriguez and Darren Hallman

Volume 1, Nº 3

March 2006

AN OFF-RESONANCE SYNCHRONOUS VIBRATION BASED METHOD FOR ROTOR SYSTEM DAMAGE DETECTION

HUAGENG LUO, HECTOR RODRIGUEZ AND DARREN HALLMAN

This paper presents a methodology for detecting rotor imbalances, such as mass imbalance and crack-induced imbalance, using shaft synchronous vibrations. A vibration detection algorithm is derived based on the first order synchronous vibration response. A detection system was integrated by using state-of-the-art commercial analysis equipment. A laboratory rotor test rig with controlled mass imbalances was used to verify the integrated system. The system was then deployed to an engine subassembly test setup. Four specimens were used in the subassembly test and the test results are reported in the final section.

1. Introduction

1.1. Mass imbalance in rotors. The physics of the mass imbalance induced vibration response in rotors can be explained using a simplified shaft-disk assembly. As shown in [Figure 1](#), a simple Jeffcott rotor is represented by a spring-mass system restricted to vibrations along the vertical y -axis. In this model, the disk is represented by its mass m , and the stiffness of the shaft is represented by k_s . This simplified representation of a rotor is typically used to model the response of single-disk rotor assemblies under relatively rigid bearings (for example, ball bearings) at relatively low speeds (that is, near or below the first bending critical speed). The response at a sensor with respect to a reference, such as a synchrophaser or a tachometer, can be represented by the response from a single-degree-of-freedom system. The amplitude of a displacement sensor response Y , at the center of the disk due to mass imbalance, is given as [\[Thomson and Dahleh 1998\]](#)

$$Y(j\omega) = \frac{U_m \omega^2}{m(\omega_0^2 - \omega^2 + 2j\xi_0\omega_0\omega)}, \quad (1)$$

where

Y is the Laplace transform of time response $y(t)$. $Y(j\omega) = L[y(t)]|_{s=j\omega}$;
 j is the complex symbol, $j = \sqrt{-1}$;

Keywords: off-resonance, synchronous vibration, damage detection, rotor system, mass imbalance, crack induced imbalance.

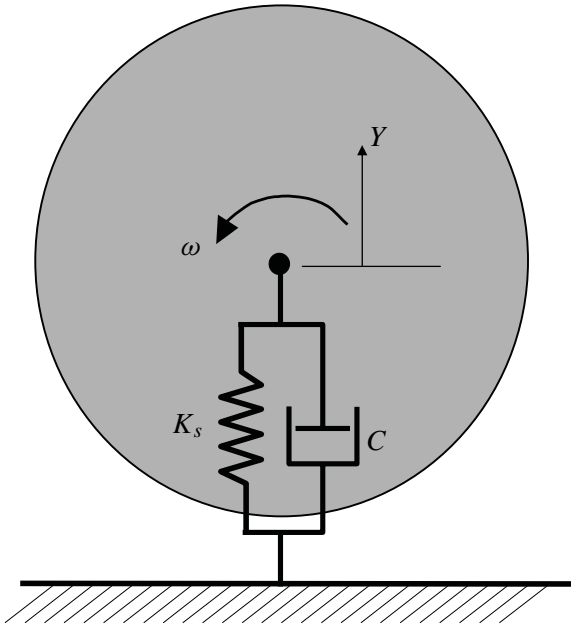


Figure 1. Jeffcott model of rotor assembly.

m is the mass of the system;

U_m is the mass imbalance in frequency domain;

$\omega_0 = \sqrt{k_s/m}$ is the natural frequency of the system;

$\xi_0 = c/2\omega_0 m$ is the damping ratio of the system.

Equation (1) shows that at speeds below the critical speed (that is, $\omega/\omega_0 \ll 1.0$), the vibration response due to mass imbalance is proportional to ω^2 .

1.2. Crack-induced imbalance. Cracks in rotor disks have been identified as the cause of a distinct behavior in the vibration response of rotor assemblies [Imam and DeLorenzi 1988; Sonnichsen 2000]. Radial-axial cracks induce a unique vibration response as they open due to tensile hoop stresses caused by centrifugal loading. The crack, which opens as a function of the square of the rotor speed, forces a redistribution of the disk mass. This redistribution results in an additional imbalance that is also proportional to the square of the speed, and hence the resulting crack-induced imbalance force is proportional to the fourth power of the shaft speed. This unique imbalance force characteristic contrasts with the force due to standard mass imbalance, which is related to the square of the shaft speed.

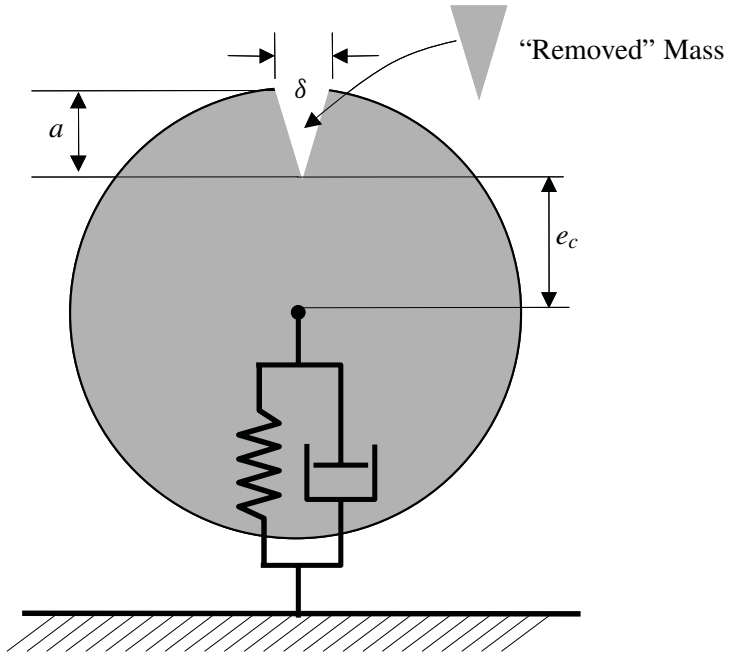


Figure 2. Jeffcott rotor showing “removed” mass concept.

In the case of a radial-axial crack with length a in a disk rotating at speed ω , the induced imbalance can be expressed as

$$U_c(a, \omega) = m_c(a, \omega)e_c, \tag{2}$$

where the effective change in mass distribution due to the crack opening $m_c(a, \omega)$ is a function of the crack size and speed, and e_c is the effective radius of rotation of $m_c(a, \omega)$. The hoop stress in a rotating disk is a function of the square of the shaft speed ω . Therefore, the effective change in mass distribution due to the crack opening is also a function of the square of the shaft speed. The response of a Jeffcott type rotor with a radial-axial crack can be obtained after substituting $U_c(a, \omega)$ for U_m in Equation (1). Due to the dependence of $U_c(a, \omega)$ on ω^2 , the resulting displacement response in the low-speed regime (that is, below the critical speed) will be proportional to the fourth power of the speed.

An approximate expression for Equation (2) can be obtained if the effective change in mass distribution due to the crack opening is represented as a “removed” mass while e_c is the radial distance to the crack tip as shown in Figure 2. In the case of a radial-axial crack, the removed mass is proportional to the opening of the crack δ as a function of speed. The opening of a small crack in a large-diameter disk can be approximated using the analogy of an edge crack in a plate strip, for

which a closed-form solution exists. The opening of the crack due to tensile hoop stress level in the neighborhood of the crack is given as [Tada et al. 1985]

$$\delta = \frac{4\sigma_h a}{E} V\left(\frac{a}{D}\right), \quad (3)$$

where the empirical function $V\left(\frac{a}{D}\right)$ is given as [Tada et al. 1985]

$$V\left(\frac{a}{D}\right) = \frac{1.46 + 3.42 \times \left(1 - \cos\left(\frac{\pi a}{2D}\right)\right)}{\left(\cos\left(\frac{\pi a}{2D}\right)\right)^2}, \quad (4)$$

where the disk diameter is used instead of the plates width, as considered in the reference. As we see in Equation (4), $V\left(\frac{a}{D}\right)$ approaches the constant value of 1.46 for small ratios of $\frac{a}{D}$.

The hoop stress in a constant thickness disk at a distance e_c is given as [NASA 1975]

$$\sigma_h = \frac{\rho D^2 \omega^2 (3 + \mu)}{32g} \left(1 - \frac{(1 + 3\mu)}{3 + \mu} \times \left(\frac{2e_c}{D}\right)^2\right), \quad (5)$$

where g is the gravity constant. Finally, the removed mass can be approximated as

$$m_c = \frac{\delta a t \rho}{2g}. \quad (6)$$

Therefore, the crack-induced imbalance is given as [Rodriguez et al. 2001]

$$U_c = K \rho^2 a^2 t D^2 \omega^2 e_c = K_C \omega^2, \quad (7)$$

where

$$K_C = \frac{(3 + \mu)}{16g^2 E} \left[1 - \frac{(1 + 3\mu)}{3 + \mu} \times \left(\frac{2e_c}{D}\right)^2\right] V\left(\frac{a}{D}\right) \rho^2 a^2 t D^2 e_c. \quad (8)$$

In the case of values of $\frac{a}{D}$ less than 0.05, Equation (8) becomes $K_C \sim 0.5/E$.

Equation (7) clearly establishes the dependence of the crack-induced imbalance on the physical parameters of the disk and the rotational speed. As shown in the equation, the crack-induced imbalance is proportional to the second power of the speed, the weight density, the crack length, and the disk diameter, respectively. In addition, for the case of relatively small cracks, e_c approximates $D/2$, introducing a stronger dependence of the imbalance on the disk diameter. Refer to references [Butz and Rodriguez 1999] and [Rodriguez et al. 2001] for more numerical simulations and analyses.

1.3. Multi-DOF modeling. It has been well established that the mass-induced synchronous vibration is proportional to the square of the rotational speed, that is, ω^2 , in the region where $\omega \ll \omega_0$, where ω_0 is the first resonant frequency of the machinery system. The radial-axial cracks in the rotating disk or shaft can cause

a synchronous vibration that is proportional to ω^4 , under the same assumption of $\omega \ll \omega_0$. Several groups have developed detection systems based on these assumptions [Imam and DeLorenzi 1988; Sonnichsen 2000]. However, in reality, there are several major difficulties in implementing the traditional algorithms:

- (i) It is difficult to satisfy the $\omega \ll \omega_0$ condition without significantly reducing the signal to noise ratio, because the first natural frequency in many rotational machinery systems is usually low. Especially in soft-mounted rotor systems, where the first natural frequency can be so low that it prevents such monitoring systems from getting meaningful results.
- (ii) It is difficult to simplify real rotor machinery into a single degree of freedom (SDOF) system. On top of the bearing DOFs, the vibration sensors are usually mounted on the bearing case or engine case, so that additional structural resonances, besides rotor-shaft resonances, may be picked up, thus destroying the polynomial relationship established for low frequency region.
- (iii) The operational frequency range is not always below first resonance frequency of the rotor machinery system.

In the next section, a nonresonant synchronous vibration based detection algorithm is developed for any operational speed region between two consecutive natural frequencies of a machinery system. The development is based on multi-degree of freedom (MDOF) rotor machinery assumptions.

2. Nonresonant synchronous vibration based approach

In the simplest possible model for rotor vibration analysis, the system is described by a spring-mass-damper single-degree-of-freedom (SDOF) system as shown in Figure 1. If there are both mass and crack-induced imbalances, by combining Equation (1) and (7), we have

$$Y(j\omega) = \frac{U_m \omega^2}{m(\omega_0^2 - \omega^2 + 2j\xi_0 \omega_0 \omega)} + \frac{K_C \omega^4}{m(\omega_0^2 - \omega^2 + 2j\xi_0 \omega_0 \omega)}. \quad (9)$$

In the region where $\omega \ll \omega_0$, Equation (9) can be simplified as

$$Y(j\omega) = \frac{U_m \omega^2}{m\omega_0^2} + \frac{K_C \omega^4}{m\omega_0^2} = C_2 \omega^2 + C_3 \omega^4, \quad (10)$$

where

$$C_2 = \frac{U_m}{m\omega_0^2} \quad \text{and} \quad C_3 = \frac{K_C}{m\omega_0^2} \quad (11)$$

are the imbalance and system parameter related complex constants.

In many cases, the rotor system response has to be modified into a multi-degree-of-freedom (MDOF) system, assuming the system has distinct natural frequencies for simplicity, as

$$Y(j\omega) = \sum_{i=1}^{\infty} \frac{U_{mi}\omega^2}{m_i(\omega_i^2 - \omega^2 + 2j\xi_i\omega_i\omega)} + \sum_{i=1}^{\infty} \frac{K_{C_i}\omega^4}{m_i(\omega_i^2 - \omega^2 + 2j\xi_i\omega_i\omega)}, \quad (12)$$

where U_{mi} is the i -th modal response coefficient due to mass imbalance; K_{C_i} is the i -th modal response coefficient due to the crack induced imbalance; m_i is the i -th modal mass; ξ_i is the i -th modal damping ratio, and

$$\omega_1 < \omega_2 < \dots < \omega_{k-1} < \omega_k < \dots \quad (13)$$

are natural frequencies of the machinery system.

In the frequency region of $\omega_{k-1} < \omega < \omega_k$, the variables

$$\frac{\omega_i}{\omega}, \quad i = 1, 2, \dots, k-1 \quad \text{and} \quad \frac{\omega}{\omega_i}, \quad i = k, k+1, \dots \quad (14)$$

are less than 1. If these quantities are much less than unity, Equation (12) can be approximated as

$$\begin{aligned} Y(j\omega) = & \sum_{i=1}^{k-1} \frac{U_{mi}\omega^2}{m_i} \frac{1}{\omega^2 \left[\left(\frac{\omega_i}{\omega}\right)^2 - 1 + 2j\xi_i \left(\frac{\omega_i}{\omega}\right) \right]} + \sum_{i=k}^{\infty} \frac{U_{mi}\omega^2}{m_i} \frac{1}{\omega_i^2 \left[1 - \left(\frac{\omega}{\omega_i}\right)^2 + 2j\xi_i \left(\frac{\omega}{\omega_i}\right) \right]} \\ & + \sum_{i=1}^{k-1} \frac{K_{C_i}\omega^4}{m_i} \frac{1}{\omega^2 \left[\left(\frac{\omega_i}{\omega}\right)^2 - 1 + 2j\xi_i \left(\frac{\omega_i}{\omega}\right) \right]} + \sum_{i=k}^{\infty} \frac{K_{C_i}\omega^4}{m_i} \frac{1}{\omega_i^2 \left[1 - \left(\frac{\omega}{\omega_i}\right)^2 + 2j\xi_i \left(\frac{\omega}{\omega_i}\right) \right]}. \end{aligned} \quad (15)$$

Using the Taylor series expansion and retaining up to the second order of small terms, we have

$$\begin{aligned} Y(j\omega) = & \sum_{i=1}^{k-1} -\frac{U_{mi}}{m_i} \left[1 + 2j\xi_i \left(\frac{\omega_i}{\omega}\right) + (1 - 4\xi_i^2) \left(\frac{\omega_i}{\omega}\right)^2 + O\left(\frac{\omega_i}{\omega}\right)^3 \right] \\ & + \sum_{i=k}^{\infty} \frac{U_{mi}}{m_i} \left[\left(\frac{\omega}{\omega_i}\right)^2 + O\left(\frac{\omega}{\omega_i}\right)^3 \right] \\ & + \sum_{i=1}^{k-1} -\frac{K_{C_i}\omega^2}{m_i} \left[1 + 2j\xi_i \left(\frac{\omega_i}{\omega}\right) + (1 - 4\xi_i^2) \left(\frac{\omega_i}{\omega}\right)^2 + O\left(\frac{\omega_i}{\omega}\right)^3 \right] \\ & + \sum_{i=k}^{\infty} \frac{K_{C_i}\omega^2}{m_i} \left[\left(\frac{\omega}{\omega_i}\right)^2 + O\left(\frac{\omega}{\omega_i}\right)^3 \right]. \end{aligned} \quad (16)$$

2.1. Zero order approximation. By omitting the first and higher orders of small terms in Equation (16), we get a zero order approximation as

$$Y(j\omega) = -\sum_{i=1}^{k-1} \frac{U_{mi}}{m_i} - \sum_{i=1}^{k-1} \frac{K_{C_i}\omega^2}{m_i}. \quad (17)$$

In the case of $k = 2$, which means the operation speed range is between the first and second resonant frequencies, Equation (17) is further simplified as

$$Y(j\omega) = -\frac{U_{m1}}{m_1} - \frac{K_{C1}\omega^2}{m_1}. \quad (18)$$

Keep in mind that in Equation (18), U_{m1} and K_{C1} are complex variables. Their amplitudes reflect the imbalance amounts while the phases reflect the circumferential locations. The negative signs in Equation (18) reflect the 180° phase shift after the first resonance.

2.2. First order approximation. By omitting the second and higher orders of small terms in Equation (16), we get a first order approximation as

$$Y(j\omega) = \sum_{i=1}^{k-1} -\frac{U_{mi}}{m_i} \left[1 + 2j\xi_i \left(\frac{\omega_i}{\omega} \right) \right] + \sum_{i=1}^{k-1} -\frac{K_{C_i}\omega^2}{m_i} \left[1 + 2j\xi_i \left(\frac{\omega_i}{\omega} \right) \right]. \quad (19)$$

In a lightly damped case, ξ_i is small, thus Equation (19) can be further reduced to Equation (17), that is, the zero order case. Therefore, in a lightly damped case, zero order and first order approximations have the same formula.

2.3. Higher order approximation. Using the Taylor series expansion, any higher-order approximation can be derived. For example, by omitting the third and higher order of small terms, we have the second order approximation:

$$Y(j\omega) = \sum_{i=1}^{k-1} -\frac{U_{mi}}{m_i} \left[1 + 2j\xi_i \left(\frac{\omega_i}{\omega} \right) + (1 - 4\xi_i^2) \left(\frac{\omega_i}{\omega} \right)^2 \right] + \sum_{i=k}^{\infty} \frac{U_{mi}}{m_i} \left(\frac{\omega}{\omega_i} \right)^2 + \sum_{i=1}^{k-1} -\frac{K_{C_i}\omega^2}{m_i} \left[1 + 2j\xi_i \left(\frac{\omega_i}{\omega} \right) + (1 - 4\xi_i^2) \left(\frac{\omega_i}{\omega} \right)^2 \right] + \sum_{i=k}^{\infty} \frac{K_{C_i}\omega^2}{m_i} \left(\frac{\omega}{\omega_i} \right)^2. \quad (20)$$

In a lightly damped case, Equation (20) can be further reduced to

$$Y(j\omega) = \sum_{i=1}^{k-1} -\frac{U_{mi}}{m_i} \left[1 + 2j\xi_i \left(\frac{\omega_i}{\omega} \right) + \left(\frac{\omega_i}{\omega} \right)^2 \right] + \sum_{i=k}^{\infty} \frac{U_{mi}}{m_i} \left(\frac{\omega}{\omega_i} \right)^2 + \sum_{i=1}^{k-1} -\frac{K_{C_i}\omega^2}{m_i} \left[1 + 2j\xi_i \left(\frac{\omega_i}{\omega} \right) + \left(\frac{\omega_i}{\omega} \right)^2 \right] + \sum_{i=k}^{\infty} \frac{K_{C_i}\omega^2}{m_i} \left(\frac{\omega}{\omega_i} \right)^2. \quad (21)$$

Rearranging Equation (21), we have

$$\begin{aligned}
 Y(j\omega) &= -\frac{1}{\omega^2} \sum_{i=1}^{k-1} \frac{U_{mi}}{m_i} \omega_i^2 - \frac{1}{\omega} \sum_{i=1}^{k-1} \frac{U_{mi}}{m_i} 2j\xi_i \omega_i - \left(\sum_{i=1}^{k-1} \frac{U_{mi}}{m_i} + \sum_{i=1}^{k-1} \frac{K_{C_i}}{m_i} \omega_i^2 \right) \\
 &\quad - \omega \sum_{i=1}^{k-1} \frac{K_{C_i}}{m_i} 2j\xi_i \omega_i + \omega^2 \left(\sum_{i=k}^{\infty} \frac{U_{mi}}{m_i \omega_i^2} - \sum_{i=1}^{k-1} \frac{K_{C_i}}{m_i} \right) + \omega^4 \sum_{i=k}^{\infty} \frac{K_{C_i}}{m_i \omega_i^2} \\
 &= \frac{C_{-2}}{\omega^2} + \frac{C_{-1}}{\omega} + C_0 + C_1 \omega + C_2 \omega^2 + C_4 \omega^4,
 \end{aligned} \tag{22}$$

where

$$\left\{ \begin{array}{l}
 C_{-2} = -\sum_{i=1}^{k-1} \frac{U_{mi}}{m_i} \omega_i^2, \\
 C_{-1} = -\sum_{i=1}^{k-1} \frac{U_{mi}}{m_i} 2j\xi_i \omega_i, \\
 C_0 = -\left(\sum_{i=1}^{k-1} \frac{U_{mi}}{m_i} + \sum_{i=1}^{k-1} \frac{K_{C_i}}{m_i} \omega_i^2 \right), \\
 C_1 = -\sum_{i=1}^{k-1} \frac{K_{C_i}}{m_i} 2j\xi_i \omega_i, \\
 C_2 = \left(\sum_{i=k}^{\infty} \frac{U_{mi}}{m_i \omega_i^2} - \sum_{i=1}^{k-1} \frac{K_{C_i}}{m_i} \right), \\
 C_4 = \sum_{i=k}^{\infty} \frac{K_{C_i}}{m_i \omega_i^2},
 \end{array} \right. \tag{23}$$

are the imbalance and system parameter related complex constants.

3. System integration

The proposed algorithm was integrated into an accelerated engine test system. In the accelerated test, it was designed to simulate an engine cycle, which consists of speed-up, dwell, and coast-down segments simulating aircraft taking-off, cruise, and landing, in a short time. For example, the speed-up process in our accelerated test was only 15 seconds. Thus, it is very important to have a system that can handle data acquisition, pre- and post-processing, and data management in a short time. In addition, the signal from such tests is usually noisy, thus it is also critical to have a processing technique to improve the signal to noise ratio.

After a careful market search, the Pulse system by B&K was selected as the hardware platform, the Production Test Advisor (PTA) by Signalysis, Inc. was selected as the database management system, and a MATLAB-based post-processing system was developed in-house and integrated into the system for real-time health monitoring.

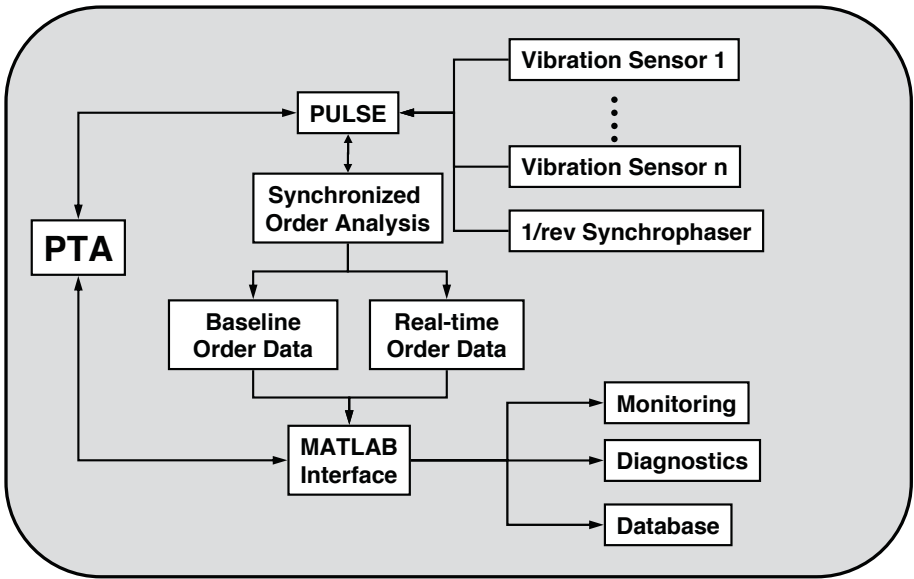


Figure 3. System diagram.

A brief system diagram is shown in [Figure 3](#). In system integration, any vibration sensors, such as accelerometers, velocity sensors, or displacement probes, can be used to pick up vibration signals for the system. Appropriate signal conditioners are needed for the sensors. A once-per-revolution (1/rev) signal from the rotating shaft is also required for order analysis and extraction.

The B&K Pulse system was used as a data acquisition and signal processing system. The Order Analyzer of the Pulse system was activated for our integrations. In order to improve the signal-to-noise ratio, a synchronous averaging technique was also employed.

Data management for the system was carried out by the PTA, which is a special version of SigQC developed by Signalysis Inc. The SigQC was originally designed for manufacturer quality assurance. It is a production line test that responds to the demand among manufacturers to automate a process for accepting or rejecting units on the assembly line based on measured noise and vibration data. The SigQC provides basic statistics, criteria, strategies and pass/fail methods. The major functions of the PTA include Database Management (Database tree) and Production Line Interface (traffic control).

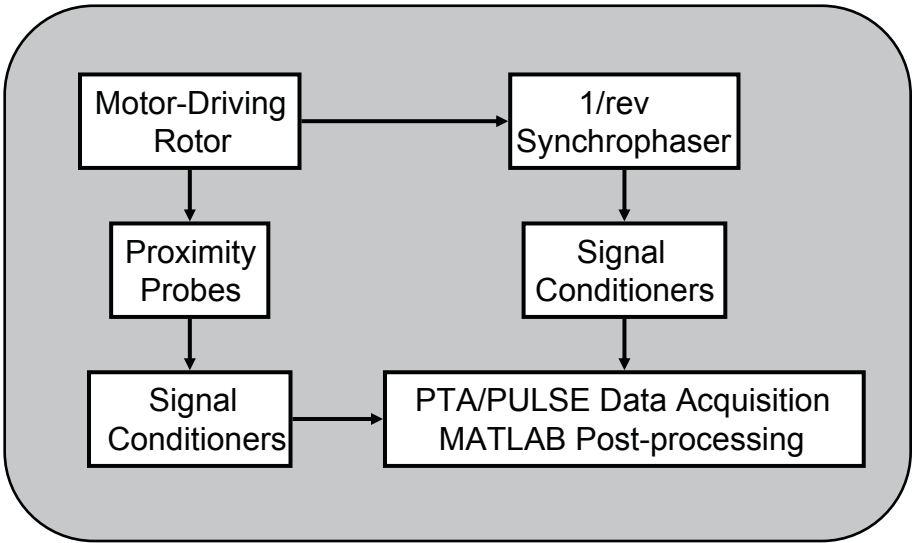


Figure 4. Small rotor rig test diagram.

Though the PTA provides basic statistics, criteria, strategies and pass/fail methods, it is very difficult, if not infeasible, to use these basic functions in constructing a diagnostic algorithm for our crack detection applications. Thus, MATLAB codes for mass and crack imbalance detection functions were developed according to equations in [Section 2](#) for nonresonant synchronous vibrations. The codes were incorporated into the crack detection system by utilizing the interface between PTA and MATLAB.

4. Small rotor test

To verify the crack detection system integration and algorithms, a Bently Nevada RK 4 rotor kit was used as a test bench.

4.1. Setup. The test rig diagram and instrument setup are shown in [Figure 4](#) and [Figure 5](#), respectively. A single rotor disk with two bearings was used. The rotor disk has a weight of 810 g. The balance slots was located at radius of 30.5 mm with 22.5° resolution in circumference (refer to [Figure 6](#)). The rotor shaft has a diameter of 10 mm. The bearing span is 400 mm with additional 200 mm overhang. With such setup, the fundamental frequency of the system is at 2000 rpm. Modal test indicates that the second bending resonance is above 167 Hz, or over 10,000 rpm.

Proximity probes were used as the signal pick-up. Sensor #1 (vib1) is in the vertical direction, while sensor #2 (vib2) is in the horizontal direction. Typical

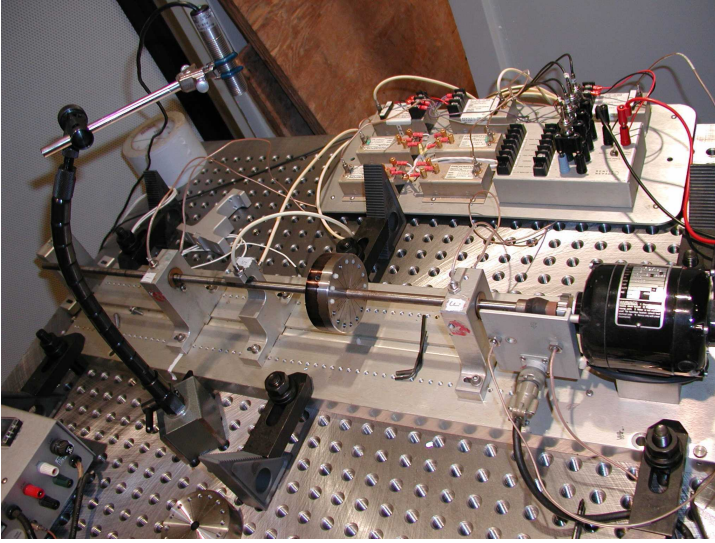


Figure 5. BN RK 4 rotor kit.

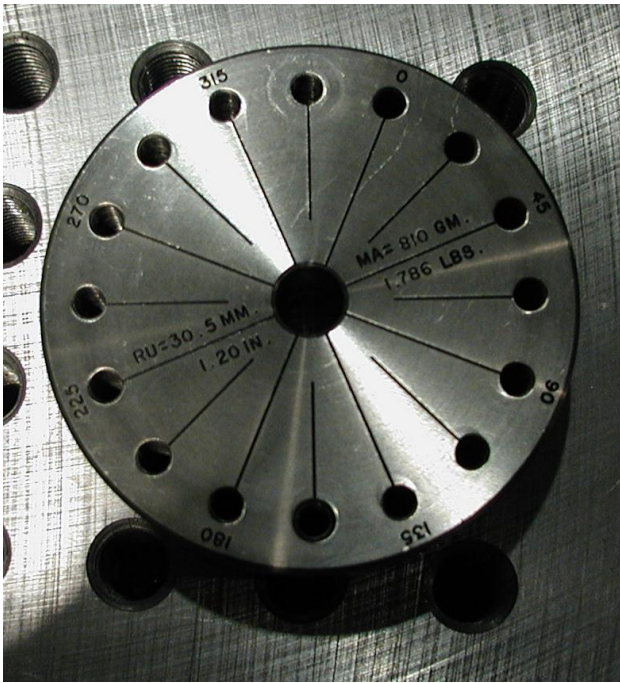


Figure 6. Rotor kit disk with balance slots.

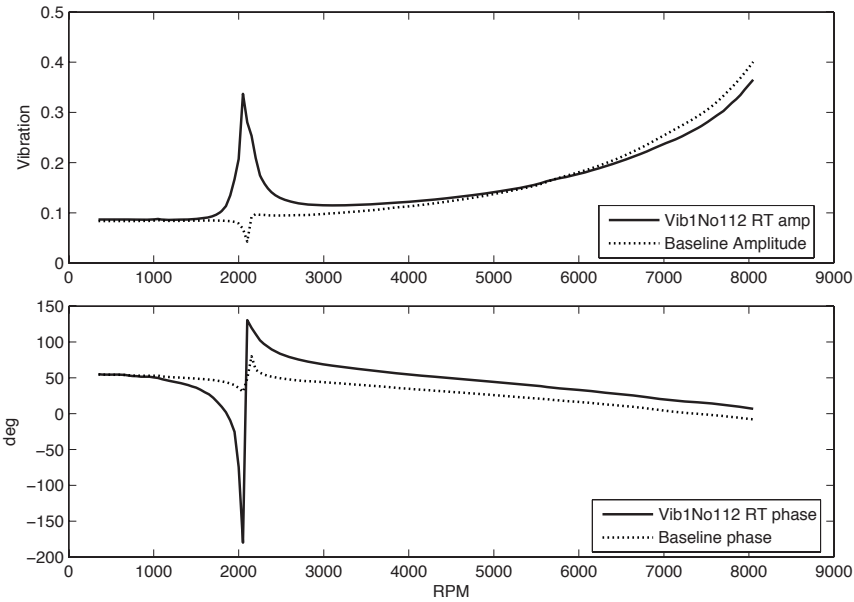


Figure 7. Typical synchronous response, vertical.

synchronous responses of the system are shown in [Figure 7](#) and [Figure 8](#), respectively.

Nylon (instead of steel) set screws were used as imbalance weights to improve the imbalance resolution. As a result, the smallest imbalance unit is 3.416 g-mm.

The disk 0° position was aligned with the center of the notch on the rotor shaft. A mechanical 1/rev signal (shaft notch detected by proximity probe) was used as the trigger. The rising edge of the signal was used as the trigger for data acquisition, which turned out to be the trailing edge of the shaft notch. Later, a laser calibration indicated that the actual triggering point corresponded to approximately the 30° rotor disk circumferential position.

4.2. Tests. The initial system was balanced first using the influence coefficient method. To verify the system integration and algorithms, imbalances were added at two circumferential positions: nominal 0° and 90° on the rotor disk. The 1/rev signal came from a notch at the shaft near the 0° mark. The actual notch was a filing-off of the shaft, which covered approximately 60° of the shaft circumference. According to the calibration, the nominal 0° and 90° circumferential positions corresponded to approximately 30° and 120° with respect to the 1/rev trigger. At each circumferential location, 4 different imbalance amounts were added: 1, 2, 3,

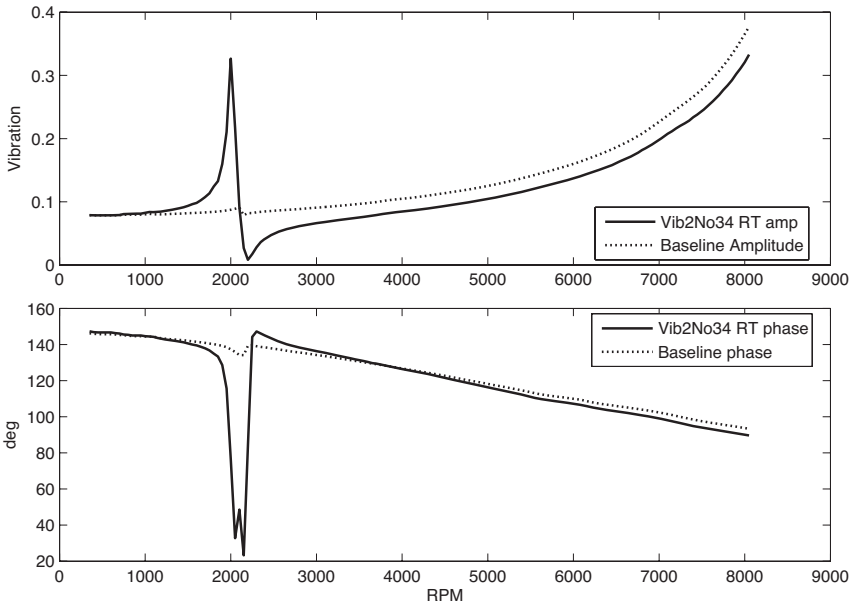


Figure 8. Typical synchronous response, horizontal.

and 4 set screws, which correspond to 3.416, 6.832, 10.248, and 13.664 g-mm imbalances.

The motor speed was controlled between 350 rpm to 8050 rpm, and 25 baseline runs were recorded. For each imbalance case, 5 repeated runs were recorded for further analysis. After that, the tests were repeated for 10 baseline conditions and 5 imbalanced runs for each imbalance case for the purpose of verification.

4.3. Data reduction. For nonresonant based analysis, the data in the speed range of 4000 to 4500 rpm were used. With this speed range, the variables in Equation (14) satisfy

$$\frac{\omega_1}{\omega} \leq 0.5 \quad \text{and} \quad \frac{\omega}{\omega_2} < 0.5.$$

Equation (19) (the first order approximation) was used in the data processing. Before curve fitting, the baseline response was subtracted from a real-time measurement in the complex domain. The difference was then used in the complex domain curve fitting for extracting the mass imbalance coefficient and the crack-induced imbalance coefficient.

The magnitudes of the typical real time measurement, the baseline, and the difference are shown in Figure 9. As can be seen from the figure, in the difference signal, the “slow roll” effect introduced by the shaft geometric imperfection has been removed after complex domain baseline subtraction. The curve fitting was

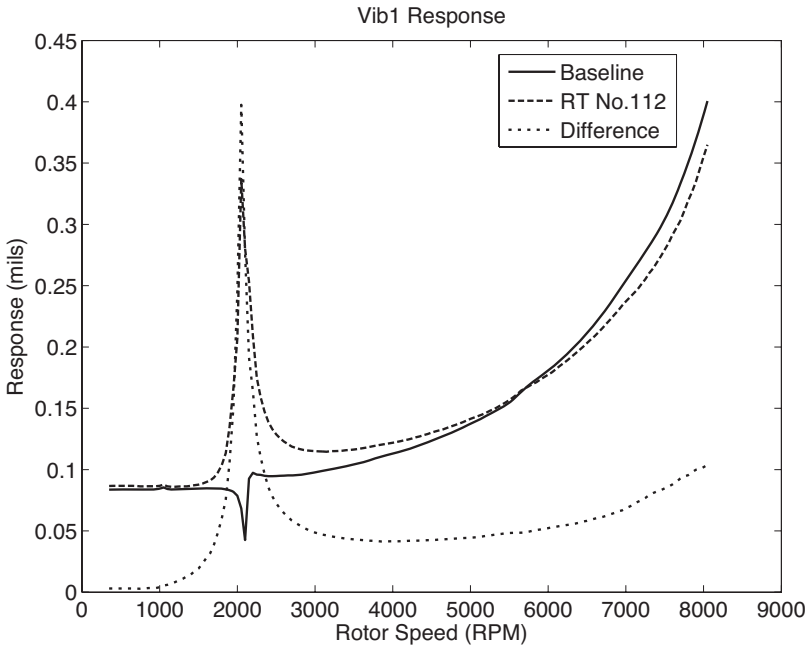


Figure 9. A typical speed-up run.

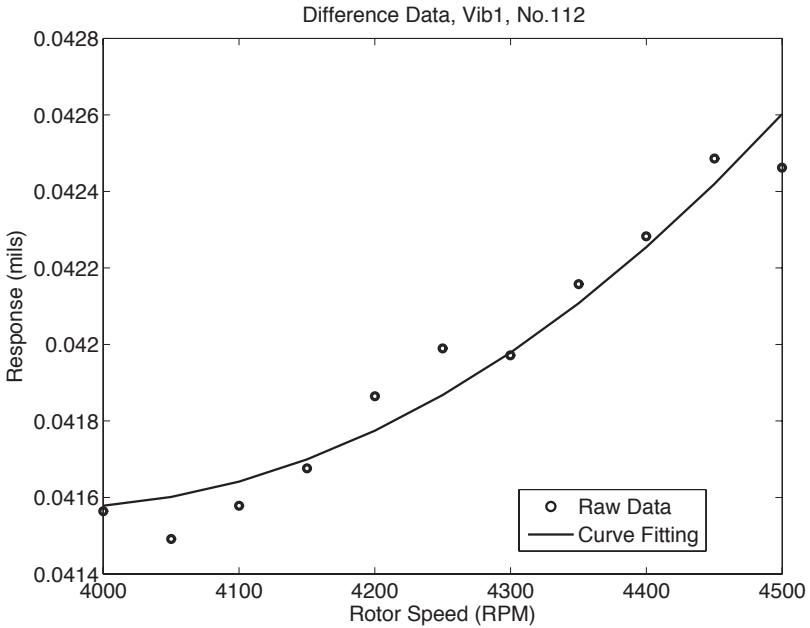


Figure 10. Curve fitting results.

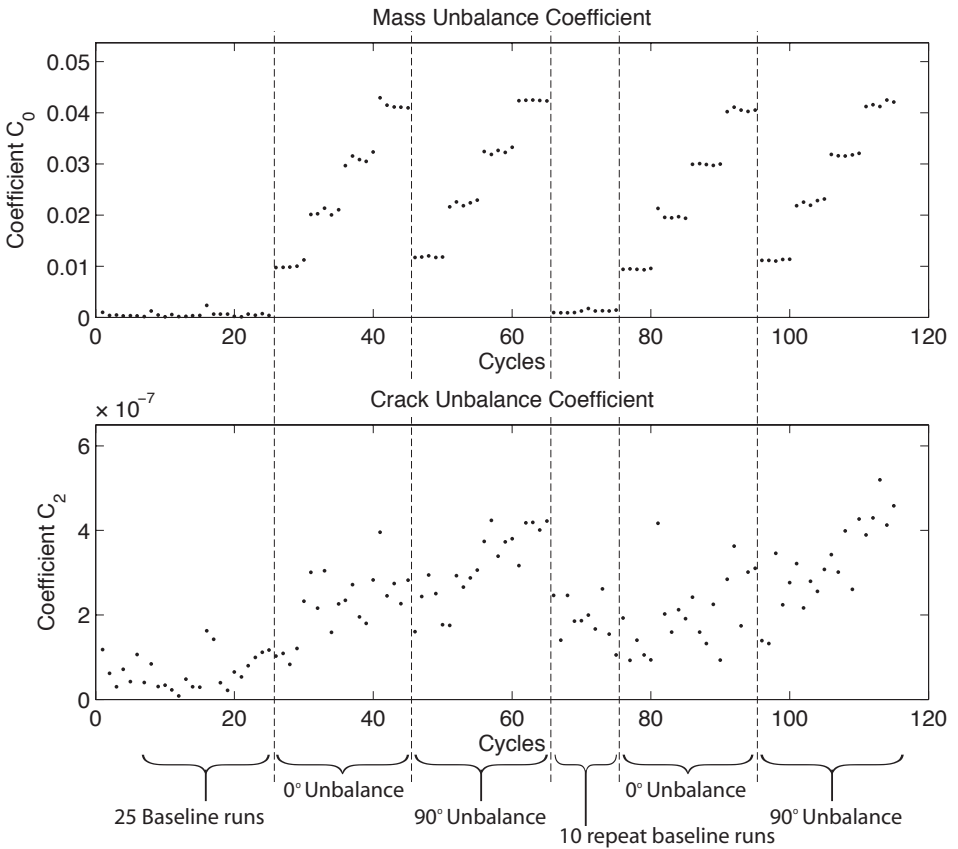


Figure 11. Nonresonance-based analysis, vertical sensor.

carried out in the complex domain with least-square minimization of the difference between the raw data and the fitting curve in the specified RPM range. A typical example of the curve fitting results is shown in Figure 10, where the solid line is the curve fitting results and the dots are the test data.

The result from the vertical sensor is shown in Figure 11, where C_0 is the mass imbalance indicator and C_2 is the crack-induced imbalance indicator. This test had 115 speed-up runs. The first 25 runs are the baseline runs. The mean of these 25 runs are the reference of the rotor health condition. The next 20 runs were the nominal 0° unbalanced runs. 1, 2, 3 and 4 nylon set crews were added to the 0° mark on the rotor. For each unbalanced case, five runs were repeated.

The next 20 runs were the nominal 90° unbalanced runs. In this case, the imbalance masses were removed from the 0° location. 1, 2, 3 and 4 nylon set crews were added to the 90° mark on the rotor. For each unbalanced case, five runs were repeated.

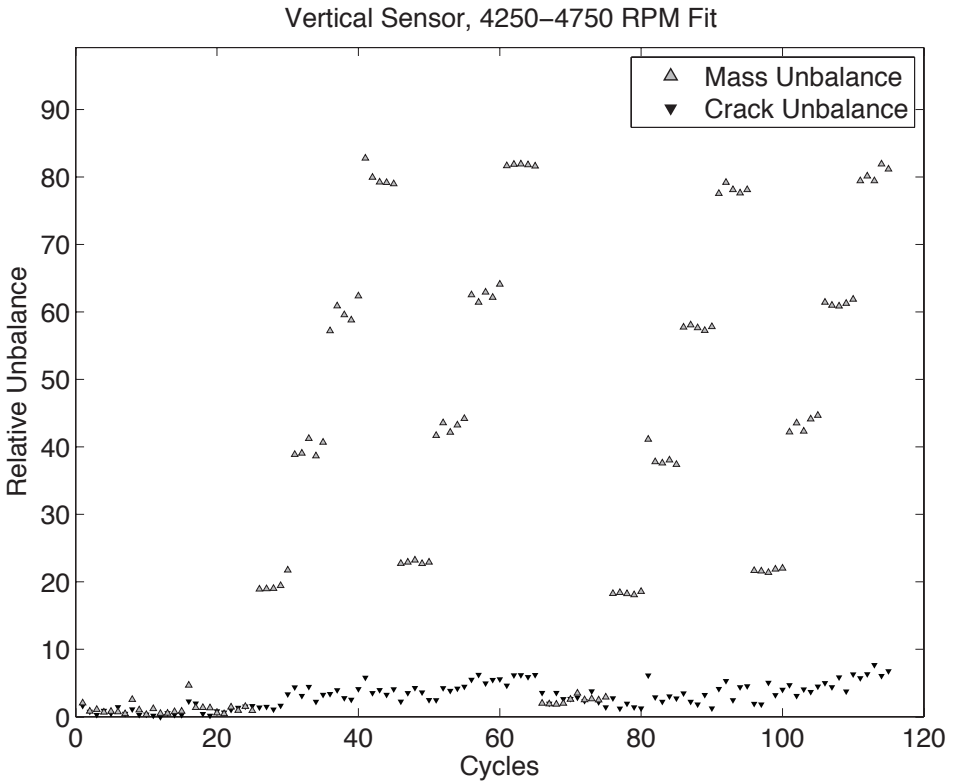


Figure 12. Identified imbalances normalized w.r.t. baseline.

To double-check the test, the procedure was repeated with 10 baseline runs, 20 nominal 0° unbalanced runs, and 20 nominal 90° unbalanced runs at different imbalance levels.

In Figure 11, the top half of the figure displays the mass imbalance parameter C_0 and the bottom half is the crack-induced imbalance parameter C_2 . We see that that the mass imbalance indicator C_0 is proportional to the imbalance added, while the crack-induced imbalance indicator C_2 does not have obvious trend. The slight upward trend is probably due to test and curve-fitting numerical variations.

In Figure 12, the normalized C_0 and C_2 are shown for comparison. In the figure, C_0 is normalized with respect to the mean of the C_0 in the first 25 baseline runs, while C_2 is normalized with respect to the mean of the C_2 in the first 25 baseline runs. Again, the normalized C_0 is also clearly proportional to the mass imbalance added. The crack-induced imbalance indicator C_2 is small. In theory, C_2 should be a small constant. The slight increase could be due to fitting errors.

	Ref.	Vertical Sensor		Horizontal Sensor	
		0°	90°	0°	90°
3.4	3.416	3.14 (−8.2%)	3.69 (+8.2%)	3.60 (+5.3%)	3.23 (−5.3%)
6.8	6.832	6.49 (−5.0%)	7.18 (+5.1%)	6.99 (+2.2%)	6.60 (−3.4%)
10.2	10.248	9.77 (−4.7%)	10.31 (+0.6%)	10.12 (−1.3%)	9.72 (−5.1%)
13.7	13.664	13.17 (−4.6%)	13.50 (−1.2%)	13.43 (−1.7%)	12.85 (−5.9%)

Table 1. Normalized mass imbalance identification. All values in g mm; percentages in parentheses indicate error relative to the reference value (second column).

To figure out the exact imbalance amount from C_0 , the exact modal parameters, such as modal mass and mode shape, are required from the rotating system. For a quick examination, the imbalance amount can be normalized at the smallest imbalance at 0° and 90° positions. The normalized mass imbalance identification is shown in Table 1, where it can be seen that the identification error is less than 9% (for the horizontal sensor, less than 6%).

Similar data processing was carried out on the horizontal sensor. The results are shown in Table 1 and Figures 13 and 14. In this sensor, the fitting error is less than 6%. In this case, the C_2 upward trend is much less.

5. Engine subassembly spin-pit tests

The engine subassembly tests were set up at the Naval Air Warfare Center in Maryland. Tests included four F404 HPT disk subassemblies. Each disk was implanted with single/multiple flaws at known/unknown locations. Each cycle included a run-up from 1500 RPM to 18000 RPM, a dwell at high speed 18000 RPM, and a coast-down from 18000 RPM to 1500 RPM. In our system, only the speed-up synchronous data was collected and analyzed. The data acquisition diagram is shown in Figure 15. A light probe was used to pick up the 1/rev signal for synchronous data reduction. Two proximity probes were used as vibration sensors. Data acquisition and signal processing were carried out at the control room near the test laboratory. The operations were monitored through remote accesses.

The test #1 results are shown in Figure 16. The full cycle history of the mass imbalance coefficient and crack-induced imbalance coefficient are shown in Figure 16(a). In this test, the cooling plate crack was developed during the cycles. It ended up with a small piece being liberated at the cooling plate (see Figure 17). The last cycles of the mass imbalance and crack-induced imbalance coefficient are

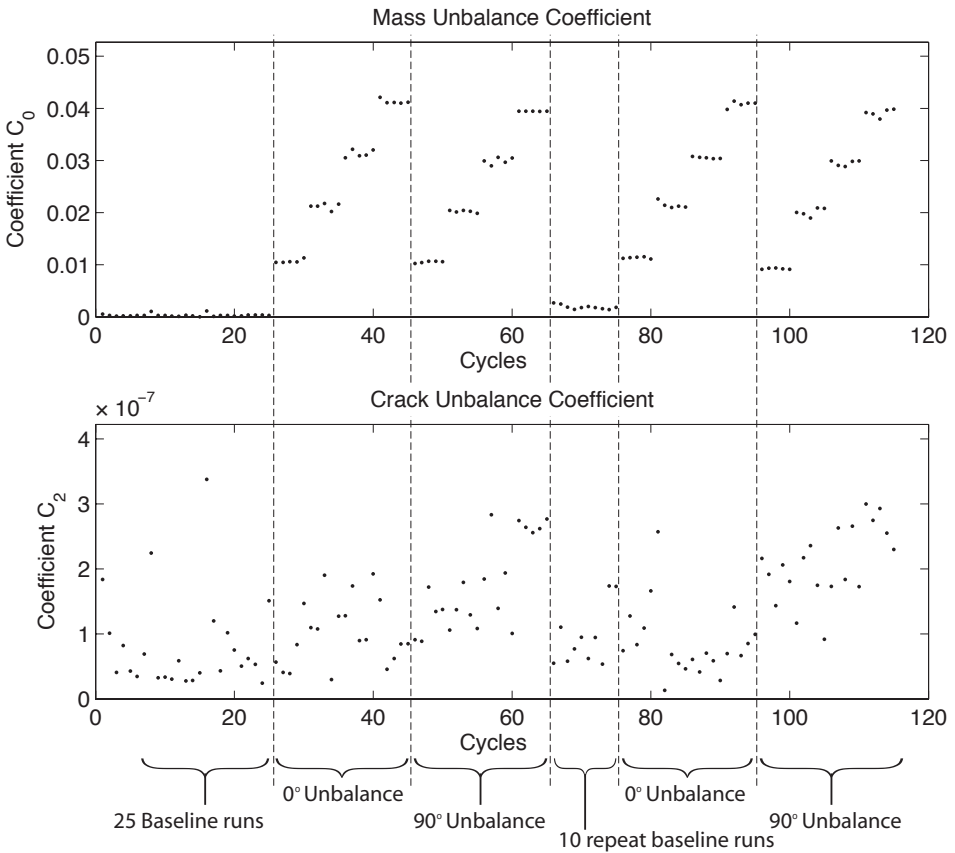


Figure 13. Nonresonance-based analysis, horizontal sensor.

shown in [Figure 16\(b\)](#), where both C_0 and C_2 coefficients increased significantly at the end of cycles.

The Test #2 results are shown in [Figure 18](#). Similar to the Test #1, the test ended after a piece of mass being liberated from the cooling plate. Again, both mass imbalance and crack-induced imbalance coefficients are significantly increased at the end of the cycle history.

The Test #3 and Test #4 results are shown in [Figure 19](#) and [Figure 20](#), respectively. In both tests, the disk crack propagated. The disks were burst at the end due to crack propagation. As seen in [Figure 19](#) and [Figure 20](#), the mass imbalance coefficients are relatively quiet in the last cycles, while the crack-induced imbalance coefficient increased gradually.

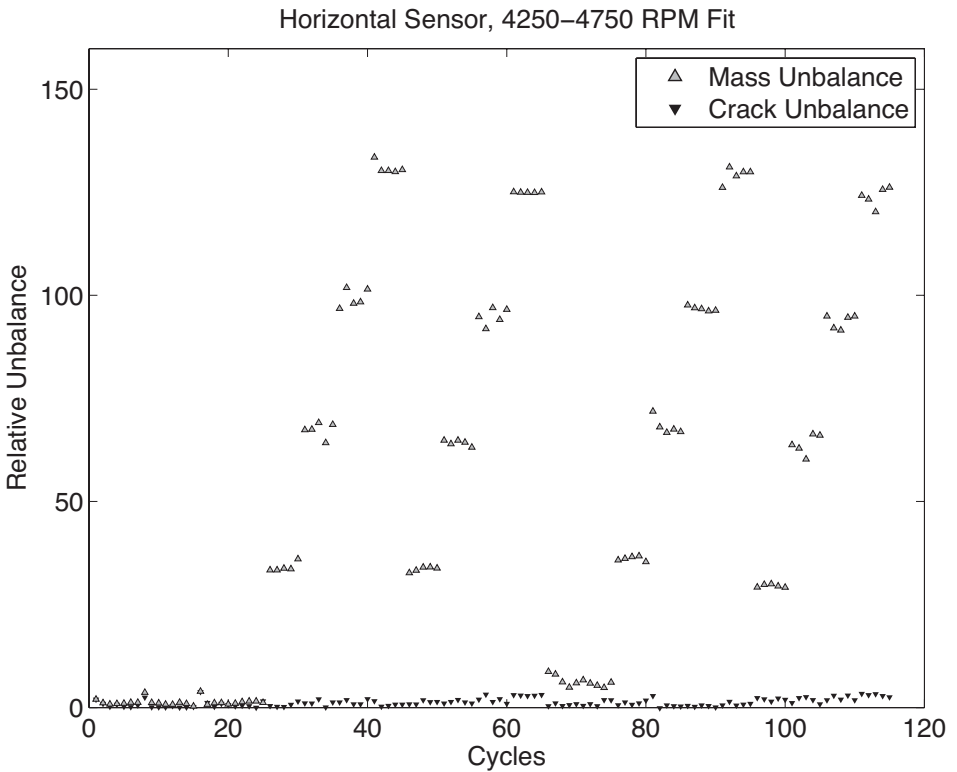


Figure 14. Identified imbalances normalized w.r.t baseline.

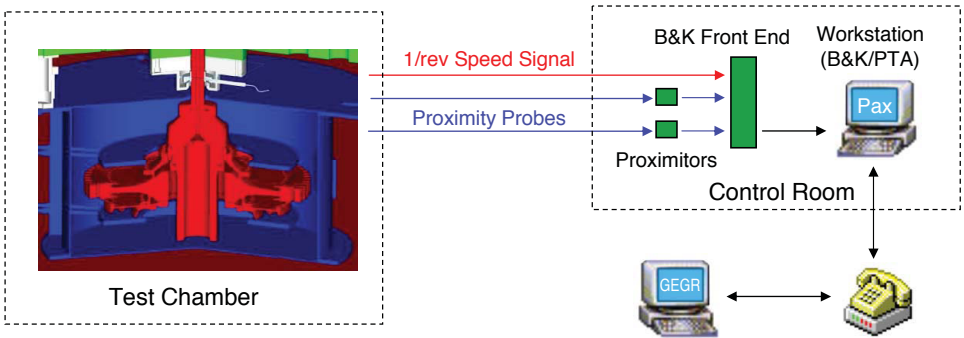


Figure 15. Engine subassembly data acquisition diagram.

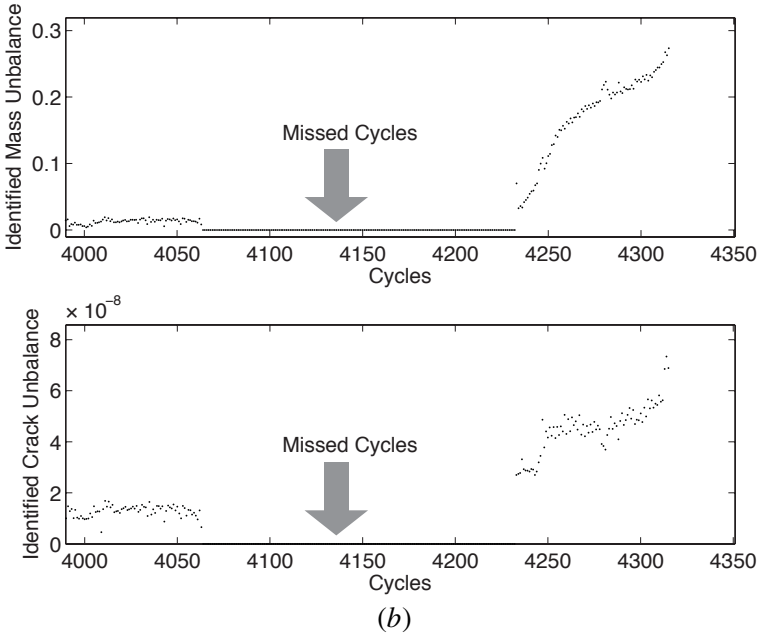
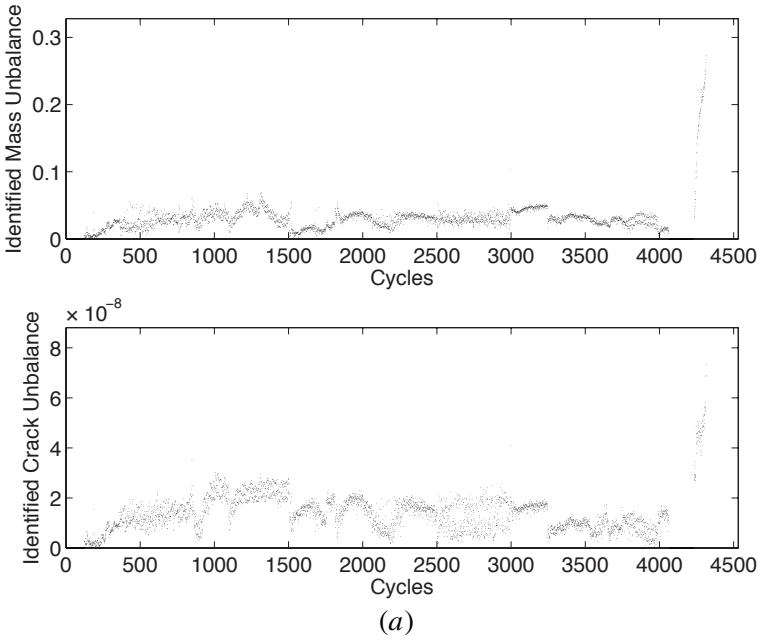


Figure 16. Test #1 results (a) all cycles and (b) last cycles.

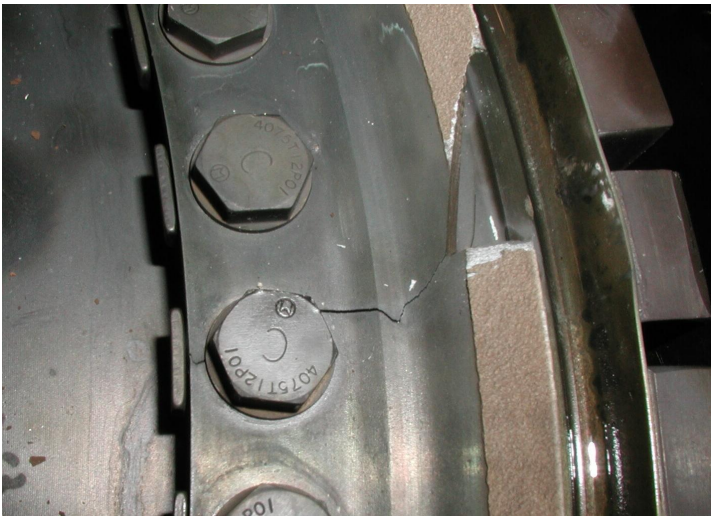


Figure 17. Crack and mass delamination at the cooling plate.

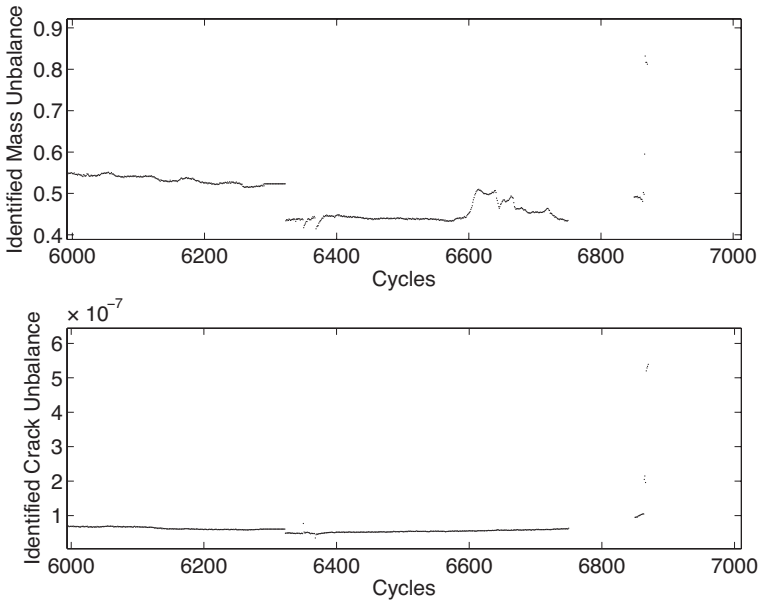


Figure 18. Test #2 results.

6. Conclusion

In this paper, an imbalance detection algorithm was derived based on rotor synchronous vibrations. Instead of an SDOF model, the multi-DOF model was used

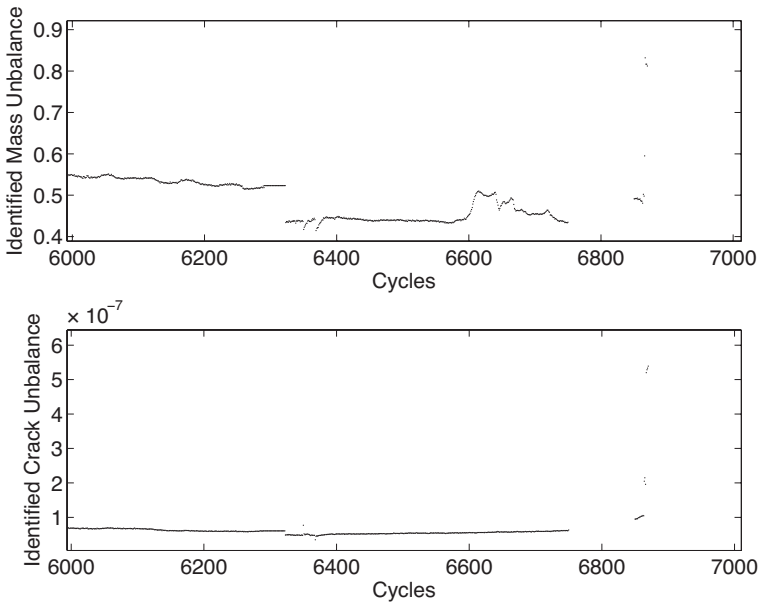


Figure 19. Test #3 results.

in the derivations. Thus, the algorithm was valid in a frequency region between any two critical speeds. The MDOF model reflected the more realistic conditions in many rotor operations. The algorithm was integrated into an automatic data collection and analysis system. The integrated system has been validated through a small rotor laboratory test rig with controlled mass imbalance and an engine subassembly with embedded disk cracks. Laboratory rig test results indicated that a good agreement between the embedded and identified imbalances can be achieved. An engine subassembly test also indicated the feasibility of trending the mass imbalance and crack-induced imbalance from the engine cycle history. Initial test results indicated that it is promising to use vibration diagnostic techniques for the online detection of engine rotor disk cracks and other anomalies. However, the sensitivity of the system needs to be improved. The precision of the 1/rev signal is also a key to the success of the algorithm.

Acknowledgments

The authors gratefully acknowledge the support of Dr. Leo Christodoulou of the Defense Advanced Research Projects Agency (DARPA), much of this work was accomplished as part of DARPA's Materials Damage Prognosis program. The authors would like to acknowledge Dennis Corbly of GE Aircraft Engines for his

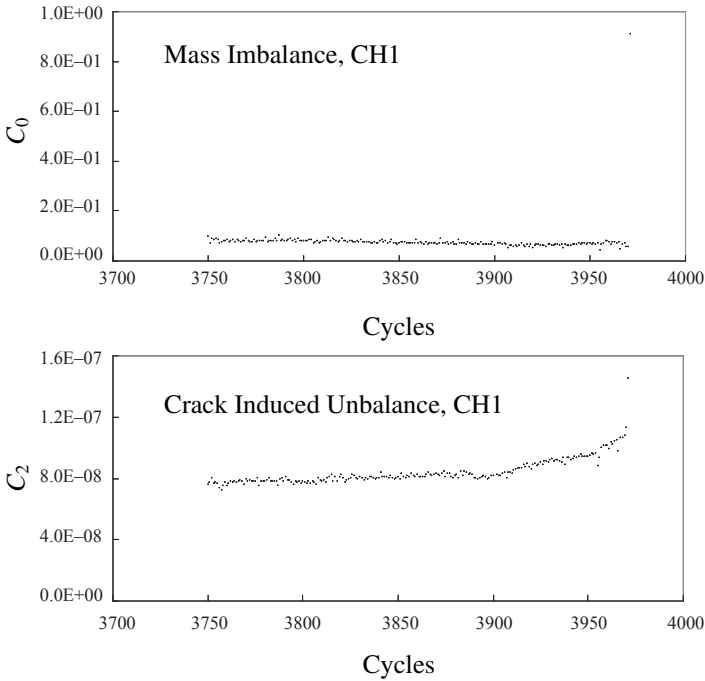


Figure 20. Test #4 results

support and leadership in the program, and Greg Muschlitz of NAWCAD for his help in the disk subassembly tests.

References

- [Butz and Rodriguez 1999] M. Butz and H. Rodriguez, "Propulsion wealth monitoring for enhanced safety", Contract NAS3-99203, NASA, Houston, TX, 1999.
- [Imam and DeLorenzi 1988] I. Imam and H. G. DeLorenzi, "Method and apparatus for detecting axial cracks in rotors for rotating machinery", *United States Patent* 4 (June 14 1988), 751,657.
- [NASA 1975] NASA, "Astronautics structures manual", NASA, Houston, TX, 1975.
- [Rodriguez et al. 2001] H. Rodriguez, D. Hallman, M. Butz, and V. Dhar, "A physics-based approach for the detection of cracks in rotating disks", Paper presented at the ISABE, 15th International Symposium on Air Breathing Engines (Bangalore, India), 2001.
- [Sonnichsen 2000] H. E. Sonnichsen, "Real-time detection of developing cracks in jet engine rotors", pp. 173–183 in *IEEE Conference*, vol. 6, 2000.
- [Tada et al. 1985] H. Tada, P. Paris, and G. Irwin, *The stress analysis of cracks handbook*, 2nd ed., Del Research Corp. and Paris Productions, St. Louis, MO, 1985.

[Thomson and Dahleh 1998] W. T. Thomson and M. D. Dahleh, *Theory of vibration with applications*, 5th ed., Prentice-Hall, Englewood Cliffs, NJ, 1998.

Received 29 Sep 2005. Revised 19 Dec 2005.

HUAGENG LUO: luoh@research.ge.com

GE Global Research Center, K1 3A 30B, One Research Circle, Niskayuna, NY 12309, United States

HECTOR RODRIGUEZ: hector.m.rodriguez@pw.utc.com

Infotech Aerospace Services, Inc., Structures Department, 699 Industrial Ave., Isabela, PR 00662, United States

DARREN HALLMAN: hallman@research.ge.com

GE Global Research Center, K1 3A 30B, One Research Circle, Niskayuna, NY 12309, United States